The Astrophysical Journal, 980:264 (15pp), 2025 February 20 https://doi.org/10.3847/1538-4357/adabbd

MUSEQuBES: The Kinematics of O VI-bearing Gas in and around Low-redshift Galaxies

Sayak Dutta[1], Sowgat Muzahid[1], Joop Schaye[2], Sebastiano Cantalupo[3], Hsiao-Wen Chen[4], and Sean Johnson[5]
[1] Inter-University Centre for Astronomy & Astrophysics, Post Bag 04, Pune 411007, India
[2] Leiden Observatory, Leiden University, PO Box 9513, NL-2300 RA Leiden, The Netherlands
[3] Department of Physics, University of Milan Bicocca, Piazza della Scienza 3, 20126, Milano, Italy
[4] Department of Astronomy & Astrophysics, The University of Chicago, 5640 S. Ellis Avenue, Chicago, IL 60637, USA
[5] Department of Astronomy, University of Michigan, 1085 S. University Avenue, Ann Arbor, MI 48109, USA
Received 2024 September 23; revised 2024 December 12; accepted 2025 January 6; published 2025 February 20

Abstract

We present a detailed study of the kinematics of O VI-bearing gas around 60 low-mass (median $\log_{10}(M_\star/M_\odot) = 8.9$) galaxies at low redshift ($0.1 < z < 0.7$) using background quasars (median impact parameter $\approx$115 kpc) as part of the MUSE Quasar-fields Blind Emitters Survey (MUSEQuBES). We find that the majority of the O VI absorbers detected within the virial radius have line-of-sight velocities smaller than the escape velocities and are thus consistent with being gravitationally bound, irrespective of the halo mass. However, the fraction of such absorbers declines at larger impact parameters. The Doppler b parameter and the velocity width (Δv_{90}) of the O VI absorbers exhibit large scatter inside the virial radius of the host galaxies, but the scatter declines sharply at impact parameter $D \gtrsim 2R_{\rm vir}$. For high-mass galaxies ($\log_{10}(M_\star/M_\odot) > 9$), O VI absorption displays a larger kinematic spread, quantified by the pixel-velocity two-point correlation function (TPCF). However, the difference becomes marginal when the pixel velocities are scaled by the galaxies' circular velocities. We do not find any significant difference between the TPCF of isolated and group galaxies when the stellar mass is controlled for. A significant fraction of groups (4/6) with four or more member galaxies do not show any detectable O VI absorption, likely due to the passive nature of the nearest galaxies.

Unified Astronomy Thesaurus concepts: Circumgalactic medium (1879); Galaxy evolution (594)

1. Introduction

The circumgalactic medium (CGM) serves as a vital reservoir of gas, influencing the life cycle of galaxies through complex interactions and exchanges of matter and energy (see J. Tumlinson et al. 2017, for a review). Due to the challenges of studying the diffuse CGM in emission, absorption-line spectroscopy using bright background sources such as quasars has become the preferred method (J. Bergeron & G. Stasińska 1986; P. Petitjean & J. Bergeron 1990). The kinematics of the absorbing gas, as imprinted in the spectra of background quasars, provides crucial information on gas flows in and around galaxies. For example, absorbers with near-solar metallicity exhibiting a large kinematic spread are thought to trace outflowing materials (e.g., T. M. Tripp et al. 2011; S. Muzahid et al. 2015; B. Rosenwasser et al. 2018). From the sign of the line-of-sight (LOS) velocity of absorption at the position of the absorber, it has been shown that the cool circumgalactic gas corotates with the galaxy, potentially representing accreting gas that is fueling the star formation (e.g., G. G. Kacprzak et al. 2010; M. T. Murphy et al. 2013; S. H. Ho et al. 2017; J. Zabl et al. 2019).

The fifth ionized state of oxygen (O^{5+} or O VI) is a favored diagnostic for studying the hotter phase of the CGM owing to its doublet nature, large oscillator strengths, and the large cosmic abundance of oxygen. Although the peak ion fraction ($f_{\rm O\,VI}$) in collisional ionization equilibrium (CIE) at $T \approx 10^{5.5}$ K makes O VI an ideal tracer for warm–hot gas, it can also trace cooler, photoionized gas in photoionization equilibrium (PIE) with ionization parameter $\log_{10} U \approx -1$. In addition, nonequilibrium processes can give rise to O VI at lower temperatures for a medium with a sufficiently short cooling time (see B. D. Oppenheimer & J. Schaye 2013).

The kinematics of O VI absorption can provide crucial information regarding its origin and its connection to host galaxies (but see G. G. Kacprzak et al. 2019). Comparing the velocity centroids and widths of the O VI absorbers with the inferred halo escape velocity of host galaxies is essential for understanding their origin(s) and the processes that drive metals far away from galaxies. Additionally, the Doppler b parameters of O VI absorption components are crucial to constrain the temperature of the gas phase giving rise to the O VI. Extensive investigations have explored the connection between bright galaxies and O VI absorption using statistically significant samples of galaxy–absorber pairs (e.g., J. X. Prochaska et al. 2011; J. Tumlinson et al. 2011; M. L. Turner et al. 2014; S. D. Johnson et al. 2015; G. G. Kacprzak et al. 2015; B. A. Keeney et al. 2017; K. Tchernyshyov et al. 2022; N. Mishra et al. 2024). The O VI abundance and kinematics around foreground $\approx L_*$ galaxies in close projection to QSO sight lines are studied in the COS-Halos survey by J. Tumlinson et al. (2011) and J. K. Werk et al. (2016). They observed that the majority of their star-forming, but not passive, galaxies exhibit O VI absorption in their CGM. This dichotomy of O VI absorption between star-forming and passive galaxies has since been reported even for stellar- and halo-mass-controlled samples in K. Tchernyshyov et al. (2023). The vast majority of the O VI absorbers in the COS-Halos sample are found to be consistent with being bound to the host halos of L_* galaxies, with LOS

velocities considerably lower than the local escape velocities. N. L. Mathes et al. (2014) and, later, M. Ng et al. (2019) found that O VI absorbers are observed to be less bound from lower-mass galaxies than from high-mass halos.

The virial temperature of the host halos of $\approx L_*$ galaxies is ideal for producing O VI in CIE. In contrast, the halos of lower-mass (sub-L_*) galaxies are too cool for collisionally ionized O VI. Cosmological simulations have predicted that strong feedback processes, such as those from star formation and active galactic nuclei (AGN), can generate significant amounts of O VI in the CGM (e.g., C. J. Liang et al. 2016). The shallower potential wells of lower-mass galaxies make them more susceptible to these feedback processes. The kinematics of circumgalactic O VI absorption carries imprints of such feedback processes. However, a comprehensive statistical sample of O VI absorption around low-mass galaxies is still lacking in the literature. Recently, state-of-the-art integral field spectrographs like MUSE (R. Bacon et al. 2010) on Very Large Telescope (VLT)/UT4 and KCWI (P. Morrissey et al. 2018) on Keck have paved the way for efficiently identifying low-mass galaxies and characterizing their environments around bright background quasars. As a consequence, the availability of O VI measurements around galaxies with a large dynamic range of stellar mass and environment is gradually increasing (see, e.g., N. Mishra et al. 2024; Z. Qu et al. 2024).

J. T. Stocke et al. (2014) and J. T. Stocke et al. (2017) found that O VI absorbers associated with groups require modeling with a few broad components, despite having an overall narrow absorption profile, compared to those associated with isolated galaxies. They attributed the broadness of the components to the warmer environment. However, the overall narrow absorption profile was explained by the inability to distribute O VI over the "circumgroup" medium, especially due to the instability of the O VI phase caused by rapid cooling. They speculated that the inability to maintain a diffuse halo of warm CGM gas gives rise to a possible interface of the diffuse hot ($T > 10^6$ K) and cooler, photoionized regions embedded in the "circumgroup" medium. Analysis based on the O VI velocity two-point correlation function (TPCF) resulted in a similar conclusion (see, e.g., S. K. Pointon et al. 2017; M. Ng et al. 2019). Since the overall kinematics of the CGM is expected to be strongly influenced by dynamical processes governed by gravity, it is crucial to study CGM absorption kinematics using stellar-mass-controlled samples.

In this paper, we investigate the kinematics of O VI-bearing gas around a unique, primarily low-mass sample of galaxies drawn from the low-z part of the MUSE Quasar-field Blind Emitters Survey (MUSEQuBES;[6] S. Dutta et al. 2024a). The relationships between host galaxy properties and column density, covering fraction, and mass of O VI-bearing gas are presented in the companion paper (Dutta et al. 2024b , hereafter Paper I). In Paper I, leveraging the detection and upper limits of O VI column density (N(O VI)), we showed that the average O VI column density, $\log_{10}\langle N\,(\mathrm{O\ VI})/\mathrm{cm}^{-2}\rangle = 14.14^{+0.09}_{-0.10}$, within the virial radius of our low-mass MUSEQuBES sample is significantly lower than that of L_* galaxies. By combining more massive star-forming galaxies from the literature with our MUSEQuBES sample, we observed that both $\langle N\,(\mathrm{O\ VI})\rangle$ and the average covering fraction peak at $\log_{10}(M_\star/M_\odot) \approx 9.5$, where the virial temperature is conducive to O VI production via collisional ionization. We further argued that photoionization and/or nonequilibrium processes are necessary for the O VI associated with low-mass dwarf galaxies ($\log_{10}(M_\star/M_\odot) < 9$). Here we explore the connection between galaxy properties and O VI kinematics using a sample of 60 galaxy–absorber pairs with detected O VI absorption.

This paper is organized as follows: In Section 2 we describe the galaxy sample used in this paper and the details of the absorption-line data and galaxy–absorber pairs. The results are presented in Section 3, followed by a discussion in Section 4. Our key findings are summarized in Section 5. Throughout the paper, we adopt a ΛCDM cosmology with $\Omega_m = 0.3$, $\Omega_\Lambda = 0.7$, and a Hubble constant of $H_0 = 70\ \mathrm{km\ s^{-1}\ Mpc^{-1}}$. All distances are in physical units unless specified otherwise.

2. Data

We investigate the connection(s) between galaxy properties and the kinematics of circumgalactic O VI-bearing gas. The absorber catalog and galaxy properties for a sample of 247 MUSEQuBES galaxies are taken from Paper I. We refer to S. Dutta et al. (2024a) for an overview of the survey design and Paper I for the results on the galaxy–absorber connection. Here we briefly discuss the galaxy and absorber properties.

2.1. Galaxy Survey

The galaxies in MUSEQuBES at low z are obtained from a blind spectroscopic redshift survey in fields centered on 16 quasars using the MUSE instrument on VLT/UT4. The 247 continuum-detected foreground galaxies have O VI coverage in high-quality Hubble Space Telescope/Cosmic Origins Spectrograph (COS) spectra of the quasars, free from contamination by geocoronal Lyα or O I emission. The redshifts of these galaxies are determined from emission (or absorption) features in the 1D spectra using MARZ (S. Hinton et al. 2016) and further refined with a modified version of the code PLATEFIT (C. A. Tremonti et al. 2004), which simultaneously fits Gaussian profiles to the available absorption and/or emission lines. Although the redshift returned by MARZ (resulting from galaxy template match) can be uncertain by $\approx$100 km s^{-1}, the refined redshift estimates of PLATEFIT are more robust (uncertainty in z obtained from the fitting errors of the Gaussian fits in PLATEFIT is $\approx$10 km s^{-1}). Comparing the redshifts of galaxies from the MUSE observation of Hubble Ultra Deep Field in nine $1' \times 1'$ shallow `MOSAIC` fields (exposure time $t_{\rm exp} \approx 10$ hr, which is somewhat higher than MUSEQuBES) with one $1' \times 1'$ `Ultra-Deep Field udf-10` (with $t_{\rm exp} \approx 30$ hr), H. Inami et al. (2017) showed that the uncertainty of spectroscopic redshifts observed with MUSE is $\approx$40 km s^{-1}. We can consider 40 km s^{-1} as the maximum redshift uncertainty of our galaxy sample for all practical purposes.

The star formation rate (SFR) is measured from the Hα or [O II] fluxes (determined by PLATEFIT; C. A. Tremonti et al. 2004) using the relations in R. C. J. Kennicutt (1998, for Hα) or L. J. Kewley et al. (2004, for O II) corrected to the G. Chabrier (2003) stellar initial mass function and corrected for dust (with Hα and Hβ line ratios). The stellar masses ($M_\star$) of these galaxies are obtained by the spectral energy distribution fitting (using FAST; M. Kriek et al. 2009) of the fluxes in 11 synthetic narrowband filters created from the full available wavelength range. Imposing a 3D friends-of-friends (FoF) algorithm with a linking velocity of $\pm$500 km s^{-1} and a linking separation of 500 kpc transverse distance enabled us to separate the galaxy

[6] The high-z counterpart of MUSEQuBES studies the gas and metals around $z \approx 3.3$ Lyα emitters (S. Muzahid et al. 2021; E. Banerjee et al. 2023).

sample into "isolated" and "group" subsamples. We use the term "group" to describe an association of two or more galaxies, without specifying the group halo mass, and we note that these structures may not necessarily be virialized.

2.2. Absorber Catalog

The O VI absorber identification in the 16 MUSEQuBES quasar fields is described in detail in Paper I. Briefly, a blind catalog of O VI absorbers in the 16 quasar spectra was created through the visual inspection of the spectra using the doublet matching technique. The column densities of the detected absorbers are obtained with Voigt profile decomposition using VPFIT (R. F. Carswell & J. K. Webb 2014). A total of 118 O VI components are detected in the redshift range $0.13 < z_{\rm abs} < 0.71$. The best-fit redshift of the fitted components ($z_{\rm comp}$) and Doppler b parameters are used to characterize the O VI-bearing gas in the CGM of the galaxies. Using the component information, an absorption *system* is defined as the collection of individual absorption components located within ± 300 km s^{-1} from each other along the LOS in a given sight line starting from the lowest-redshift component. The 118 individual components can be grouped into 67 such systems.[7] The width of an absorption system is quantified by Δv_{90}, defined as the velocity extent within which 90% of the total O VI column density of the system is recovered.

The galaxy–absorber association is obtained by cross-matching our galaxy catalog with the blind O VI absorber catalog with a linking velocity of ± 300 km s^{-1} centered on each galaxy redshift in a given MUSE field. The column densities of all absorption components within the velocity windows are summed to obtain the total column density associated with a galaxy. The $z_{\rm comp}$ and b of all the associated components are used for this study. The redshift of an absorption system ($z_{\rm sys}$) in this context is defined as the column-density-weighted mean redshift of the contributing components.[8]

Out of the 247 galaxies used in this work, 60 exhibit associated O VI absorption with a median of two components per system. Note that a single absorption system can be shared by multiple galaxies if the galaxies are closely separated along the LOS. In the left panel of Figure 1, the specific SFR (sSFR) of the galaxies is plotted against the stellar mass for the 60 galaxies with filled circles. The points are color-coded by the redshift of the galaxies. The black solid line represents the star-forming main sequence (SFMS) at $z = 0.5$ (L. A. Boogaard et al. 2018), with the gray shaded region indicating the 3σ scatter around this relation. Consistent with the findings of J. Tumlinson et al. (2011) and K. Tchernyshyov et al. (2022), the galaxies associated with the detected O VI absorptions are predominantly star-forming (within 3σ of the SFMS). In Paper I, we show that the covering fraction of star-forming galaxies is significantly enhanced compared to passive galaxies inside the $R_{\rm vir}$. However, no significant difference in covering fraction is observed beyond $R_{\rm vir}$. For our galaxy sample, $R_{\rm vir}$ is defined as the radius of a spherical region within which the mean mass density is 200 times the critical density of the universe. This is obtained from the halo mass estimated using the stellar mass and redshift measurements of galaxies adopting the abundance-matching relation from B. P. Moster et al. (2013).

In this work, we present the kinematics of the O VI-bearing phase for the 60 galaxies with detected O VI absorption, out of which 25 and 35 are classified as "isolated" and "group" galaxies, respectively. Multiple group galaxies can share a single O VI system (and the associated components). However, we have verified that assigning a unique host galaxy to the O VI absorption systems (based on the galaxy with minimum $D/R_{\rm vir}$, or minimum D, or maximum $M_\star$ within a group) does not change our conclusions (see Appendix A). The right panel of Figure 1 shows the distribution of $\log_{10}(M_\star/M_\odot)$, normalized impact parameter $D/R_{\rm vir}$, and z with blue colors. The isolated galaxy properties are indicated with red envelopes in both panels. The red hatched histograms represent the distribution of isolated galaxy properties in the right panel.

3. Results

3.1. LOS Velocity of Absorbing Gas with Respect to the Galaxy

The distribution of LOS velocity offset ($v_{\rm LOS}$) between the velocity centroid of O VI components with respect to the host galaxy redshift is shown in Figure 2 with the green histogram constructed with bins of 20 km s^{-1}. Here $v_{\rm LOS}$ is given by

$$v_{\rm LOS} = (3 \times 10^5 \,{\rm km\,s^{-1}}) \times \frac{z_{\rm comp} - z_{\rm gal}}{1 + z_{\rm comp}}. \quad (1)$$

We define $P(v_{\rm LOS})$ as the ratio of the number of O VI components in a given $v_{\rm LOS}$ bin to the total number of galaxy–absorber pairs in the sample. The red dashed line represents the best-fit Gaussian profile to the observed $v_{\rm LOS}$ distribution. The mean ($\langle v_{\rm LOS}\rangle$) and standard deviation ($\sigma_{v_{\rm LOS}}$) obtained from the best-fit Gaussian profile are $\approx 18 \pm 7$ km s^{-1} and $\approx 86 \pm 7$ km s^{-1}, respectively.

To determine the mean $P(v_{\rm LOS})$ for a random region, we cross-matched the full sample of 247 galaxies with the blind O VI component catalog on a sight-line-by-sight-line basis. We then constructed the $v_{\rm LOS}$ distribution for regions far from galaxies (i.e., $|v_{\rm LOS}| > 1000$ km s^{-1}) and calculated the mean $P(v_{\rm LOS})$ from this distribution. The mean $P(v_{\rm LOS})$ of the random region (black solid line) is also consistent with the expected O VI absorber density in a random region assuming the $d\mathcal{N}/dz$ of C. W. Danforth et al. (2016), with a threshold $N({\rm O\,VI}) = 10^{13.5}$ cm^{-2}. Strongly enhanced velocity clustering of absorbers relative to the random region is observed within $\approx \pm 200$ km s^{-1} from the host galaxy redshift.

Next, we repeat this exercise for O VI *systems* in which the absorption velocity centroid is determined from the column-density-weighted mean redshift of the associated components. Such an analysis produces consistent results ($\langle v^{\rm sys}_{\rm LOS}\rangle \approx 16 \pm 12$ km s^{-1}, $\sigma_{v^{\rm sys}_{\rm LOS}} \approx 77 \pm 12$ km s^{-1}).

It is worthwhile to mention that the 60 galaxies with detected O VI absorption in our MUSEQuBES sample have a median $\log_{10}(M_\star/M_\odot) = 8.9$, corresponding to a virial velocity of ≈ 80 km s^{-1} at $z = 0.4$. The observed $\sigma_{v_{\rm LOS}}$ is higher than the LOS component of the virial velocity ($\sigma^{\rm vir}_{\rm LOS} = 80/\sqrt{3} \approx 46$ km s^{-1}). Even considering the redshift uncertainties (Δz) of ≈ 40 km s^{-1}, the total extent due to the virial velocity and redshift uncertainties ($\Delta z^2 + (\sigma^{\rm vir}_{\rm LOS})^2 \approx 60$ km s^{-1}) is marginally lower than the observed $\sigma_{v_{\rm LOS}}$.

[7] Using a different velocity window of ± 200 and ± 400 km s^{-1} resulted in 67 and 65 absorption systems, respectively. Thus, our conclusions are not sensitive to the velocity window typically used to define Δv_{90}.

[8] The grouping of components within ± 300 km s^{-1} centered on each galaxy redshift resulted in *systems* identical to the one described in the previous paragraph with the exception of two galaxies, each having one component of a *system* lying outside ± 300 km s^{-1} from the galaxy redshift.

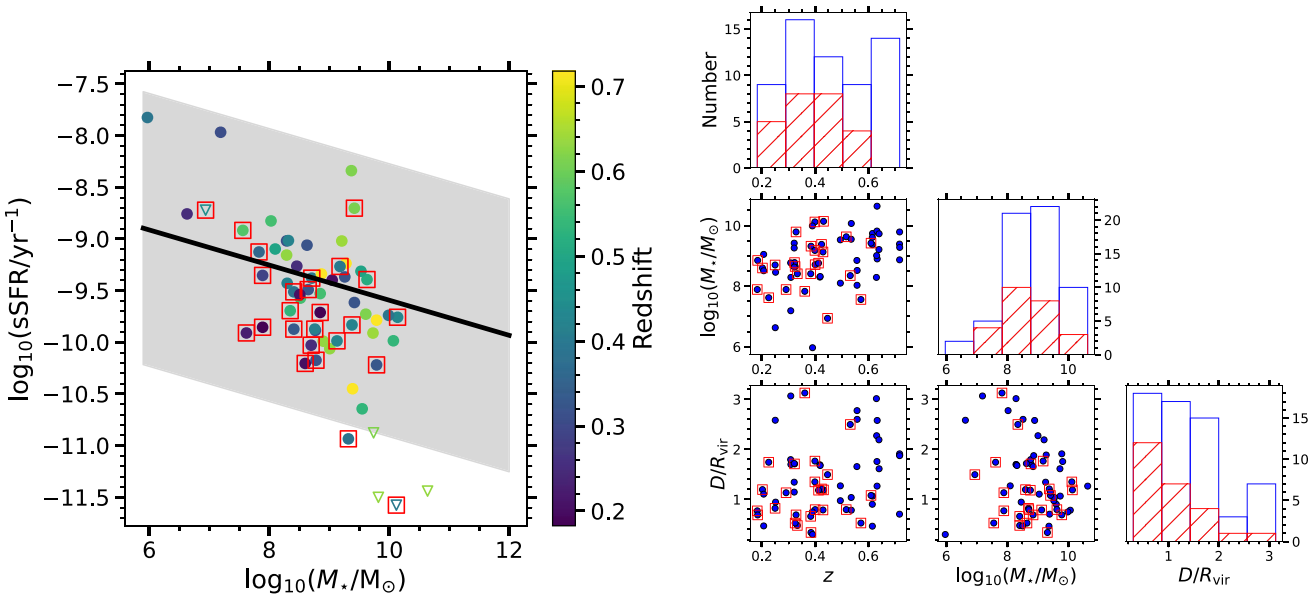

Figure 1. `Left`: the sSFR of the 60 galaxies with detected O VI absorption plotted against stellar mass. The filled circles and open triangles represent detections of and 3σ upper limits on the sSFR, respectively. The points are color-coded by the redshift of the galaxies. The SFMS relation at $z = 0.5$ and its 3σ scatter from L. A. Boogaard et al. (2018) are shown with the black solid line and the gray shaded region, respectively. The square envelopes indicate "isolated" galaxies. `Right`: the $D/R_{\rm vir}$, $\log_{10}(M_\star/M_\odot)$, and z distribution of galaxies with detected O VI absorption plotted against each other, with histograms plotted along the diagonal panels. The full sample of galaxies is shown with filled blue circles and blue solid lines, while the subsample of isolated galaxies is shown with red envelopes and red hatched histograms.

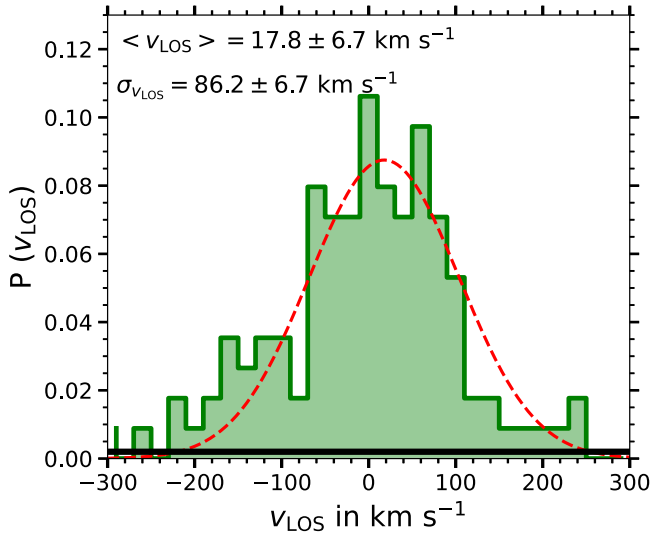

Figure 2. LOS velocity distribution of O VI components with respect to the host galaxy redshift, normalized by the number of galaxy–component pairs in the MUSEQuBES sample. The filled green histogram represents the O VI components around galaxies. The solid black horizontal line (very close to 0) represents the average absorber density in a random region (see text). The red dashed line represents the best-fit Gaussian to the observed LOS velocity distribution, with the best-fit mean ($\langle v_{\rm LOS}\rangle$) and standard deviation ($\sigma_{v_{\rm LOS}}$) indicated inside the panel.

Dividing our galaxy–absorber samples into two $D/R_{\rm vir}$ bins, we observe a significantly higher $\sigma_{v_{\rm LOS}} \approx 100\,{\rm km\,s^{-1}}$ ($\sigma_{v_{\rm LOS}}^{\rm sys} \approx 87\,{\rm km\,s^{-1}}$) for galaxies at $D > R_{\rm vir}$, compared to $\sigma_{v_{\rm LOS}} \approx 76\,{\rm km\,s^{-1}}$ ($\sigma_{v_{\rm LOS}}^{\rm sys} \approx 70\,{\rm km\,s^{-1}}$) for galaxies at $D \leqslant R_{\rm vir}$. The increase in $\sigma_{v_{\rm LOS}}$ at larger $D/R_{\rm vir}$ can be a consequence of an increasing number of background/foreground or correlated absorbers outside the halo. Restricting to the galaxies with $D \leqslant R_{\rm vir}$, we do not observe any significant difference of $\sigma_{v_{\rm LOS}}$ between high-mass ($\log_{10}(M_\star/M_\odot) \geqslant 9$) and low-mass ($\log_{10}(M_\star/M_\odot) < 9$) galaxies. We note that the observed $\sigma_{v_{\rm LOS}}^{\rm sys} \approx 70\,{\rm km\,s^{-1}}$ within $R_{\rm vir}$ for the O VI-bearing gas is consistent with the dispersion of Mg II-bearing gas around $\log_{10}(M_\star/M_\odot) \approx 9.6$ galaxies reported by Y.-H. Huang et al. (2021), despite the fact that O VI and Mg II are thought to trace two different phases of the CGM.

3.2. *Doppler* b *Parameter*

The internal kinematics of the O VI absorption can be quantified by the Doppler b parameter of individual Voigt components. In the left panel of Figure 3, we plot the b parameter of individual components against the stellar mass of host galaxies. The circles are color-coded by the sSFR of the host galaxy. The galaxies with upper limits on the sSFR are assigned the flag value[9] of $10^{-11}\,{\rm yr^{-1}}$, where the color scale saturates. Additionally, the area of the circles is proportional to the $(D/R_{\rm vir})^{-2}$ of the host galaxy. The points with small black circles in the center indicate the components associated with "isolated" galaxies in our sample. The Kendall-τ correlation coefficient indicates a weak correlation ($\tau = 0.11$, $p = 0.08$) between the b parameter and the stellar mass ($M_\star$) for the full sample, with a stronger correlation observed when considering measurements for "isolated" galaxies ($\tau = 0.25$, $p = 0.02$) only. Notably, the broad components with $b > 40\,{\rm km\,s^{-1}}$ are primarily associated with relatively massive galaxies. However, massive galaxies also exhibit components with low b values.

The b parameter includes contributions from both thermal and nonthermal or turbulent motion. A robust upper limit on the temperature can be inferred from b, as

$$b^2 = 2kT/m_{\rm O} + b_{\rm turb}^2, \qquad (2)$$

where $b_{\rm turb}$ represents the contribution from nonthermal motions and k and $m_{\rm O}$ are the Boltzmann constant and mass

[9] The actual upper limits can be higher than the flag value.

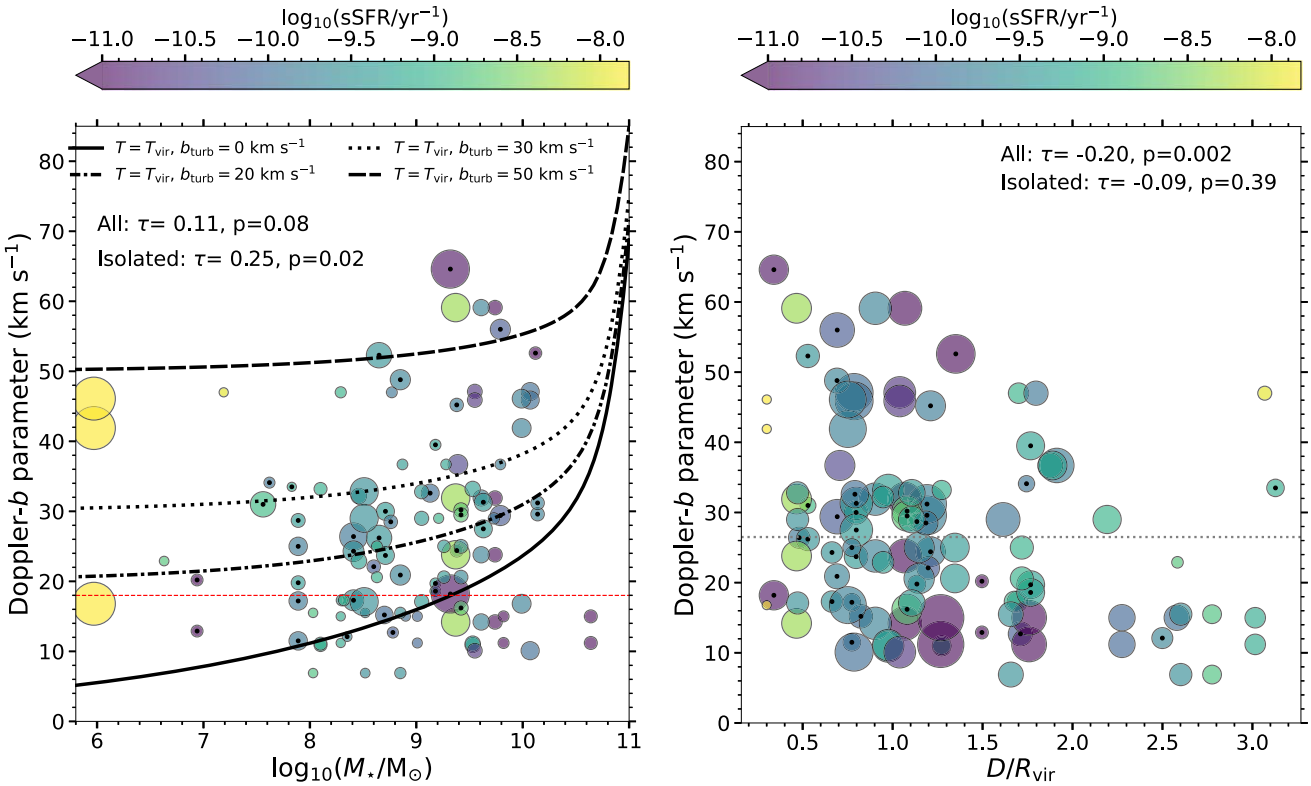

Figure 3. `Left`: b parameter of O VI components plotted against the stellar mass of the host galaxy. The circles are color-coded by the sSFR. The galaxies with upper limits on the sSFR are assigned the flag value of 10^{-11} yr^{-1}, where the color scale saturates. The area of the circles is proportional to the $(D/R_{\rm vir})^{-2}$ of the host galaxy. The absorption components hosted by isolated galaxies are marked with black circles in the center. The solid, dashed–dotted, dotted, and dashed lines represent the expected b parameter for the virial temperature of the host halo along with the turbulent velocities of 0, 20, 30, and 50 km s^{-1}, respectively. The horizontal red dashed line indicates the thermal width corresponding to the temperature at which the O VI ion fraction peaks in collisional ionization. `Right`: b parameter plotted against $D/R_{\rm vir}$ of the host galaxy. The color-coding is the same as on the left. The area of the circles is proportional to the stellar mass of the host galaxy. The horizontal gray dotted line indicates the median b value of O VI components with $\log_{10}(N\,({\rm O\ VI})/{\rm cm}^{-2}) < 14$ from C. W. Danforth et al. (2016).

of the oxygen atom, respectively. Assuming $b_{\rm turb} = 0$, conservative upper limits on the temperature can be obtained from the b parameter as $T_{\rm max} = 1.5 \times 10^6 \left(\frac{b}{40\ \ {\rm km\ \ s^{-1}}}\right)^2$ K. For galaxies with $\log_{10}(M_\star/M_\odot) < 10$, the virial temperature is $<10^6$ K. The inferred $T_{\rm max}$ for $b = 40\,{\rm km\,s^{-1}}$ is $\approx 10^6$ K, implying that the maximum allowed gas temperature is consistent with the virial temperature of the galaxies' host halos.

In the left panel of Figure 3, we show the expected O VI b parameter for gas at the virial temperature of the halo with $b_{\rm turb}$ values of 0, 20, 30, and 50 km s^{-1} in solid, dashed–dotted, dotted, and dashed lines, respectively. The virial temperature of a galaxy is determined from the halo mass, obtained using the abundance-matching relation of B. P. Moster et al. (2013). A significant fraction of the O VI components exhibits b values that are consistent with $b_{\rm turb} \geqslant 20\,{\rm km\,s^{-1}}$, assuming that the maximum attainable gas temperature is equal to the virial temperature. We will discuss turbulence in the CGM further in Section 4.2.

The red dashed line in Figure 3 indicates the b parameter corresponding to the temperature at which the O VI ion fraction peaks ($b_{\rm peak}$) in CIE (i.e., $T_{\rm peak} = 10^{5.5}$ K). A total of 19 out of the 113 components ($\approx$17%) exhibit $b + \Delta b < b_{\rm peak}$, where Δb is the 1σ error in b returned by VPFIT. This suggests that the absorbing gas for these components is cooler than the temperature required for CIE. Interestingly, 16 out of these 19 components are detected at $D \geqslant R_{\rm vir}$, as indicated by their small sizes. Moreover, out of the 20 components with $b + \Delta b$ below the solid black line, indicating the maximum thermal broadening for the virial temperature ($b(T_{\rm vir})$), 14 are associated with galaxies with $D \geqslant R_{\rm vir}$. Clearly, the majority of the O VI components are broad enough to accommodate the temperatures required for collisional ionization. The small fraction for which the b value is too low for O VI to be collisionally ionized is predominately located at $D \geqslant R_{\rm vir}$. In the outer CGM, such absorption components may arise from photoionization by the extragalactic UV background radiation.

At this point, we reiterate that a single O VI component may be associated with multiple group galaxies, resulting in counting the same component multiple times. Associating the galaxy with the smallest $D/R_{\rm vir}$ in a given group with the O VI components results in eight components with $b + \Delta b < b(T_{\rm vir})$. Four out of the eight components are hosted by galaxies with $D/R_{\rm vir} < 1$, and all of them have $\log_{10}(M_\star/M_\odot) \geqslant 9.4$.

In the right panel of Figure 3, we plot the b parameter of individual components against the $D/R_{\rm vir}$ of the associated galaxies. The size of the circles is proportional to the stellar mass of the host galaxy. Other details are similar to the left panel of Figure 3. A weak anticorrelation is observed between $D/R_{\rm vir}$ and b, with a Kendall-τ correlation coefficient of $\tau = -0.20$ ($p = 0.002$) for the full sample. No such correlation is seen for the isolated subsample ($\tau = -0.09$, $p = 0.39$). It is evident that the large b values ($b > 40\,{\rm km\,s^{-1}}$) are seen only within $\approx 2R_{\rm vir}$. The dotted horizontal line in the plot shows the median b parameter ($\approx$27 km s^{-1}) of the O VI components in

the "galaxy-blind" catalog of C. W. Danforth et al. (2016) with $\log_{10}(N(\mathrm{O\,VI})/\mathrm{cm}^{-2}) < 14$. This can be considered the median O VI b parameter in random regions. The median b value of the components within $\approx 2R_{\rm vir}$ is 26 km s^{-1}, whereas it is 15 km s^{-1} at $>2R_{\rm vir}$. It is interesting to note that the majority of the galaxies at $>2R_{\rm vir}$, which likely drives the weak anticorrelation seen for the full sample, are not isolated. A two-sample KS test reveals a marginally different b distribution for the isolated and group galaxies ($p = 0.057$), albeit with a comparable median b of $\approx$27 and 24 km s^{-1}, respectively. Restricting to galaxies with $D < R_{\rm vir}$, however, we do not observe any statistical difference in the b distributions of the isolated and group galaxies ($p = 0.196$). Finally, there is no significant color gradient in the plot, indicating that there is no evidence for a correlation between the sSFR and the gas kinematics.

3.3. Δv_{90} and TPCF

While the b parameter provides insights into the kinematics of individual components, the intercloud kinematics is better captured by the full kinematic extent of the absorption systems. The full kinematic extent of an O VI absorber can be quantified using Δv_{90} and the pixel-velocity TPCF.

We define Δv_{90} as the velocity range that encompasses 90% of the total column density of the system. In Figure 4, we plot Δv_{90} against $D/R_{\rm vir}$ of the associated galaxy. The circles are color-coded by the sSFR of the galaxy. The galaxies with upper limits on the sSFR are assigned a flag value of 10^{-11} yr^{-1}, where the color scale saturates. Additionally, the area of the circles is proportional to the stellar mass of the host galaxy. The absorption systems associated with isolated galaxies are marked with black circles in the center. The Kendall-τ correlation coefficient reveals a moderate anticorrelation ($\tau = -0.35$, $p < 0.001$) between the Δv_{90} and $D/R_{\rm vir}$ for the full sample of 60 galaxies, which vanishes when only the 25 isolated galaxies are considered. The anticorrelation is primarily driven by the high-Δv_{90} systems associated with galaxies at $D/R_{\rm vir} < 1$. The broad O VI systems ($\Delta v_{90} > 200$ km s^{-1}) are primarily associated with galaxies in groups. A Kendall-τ correlation yields a tentative, weak correlation between $\log_{10}(M_\star/M_\odot)$ and Δv_{90} with $\tau = -0.20$, $p = 0.2$ ($\tau = -0.17$, $p = 0.09$) for galaxies with $D/R_{\rm vir} < 1$ ($D/R_{\rm vir} < 2$).

The gray horizontal dotted line in Figure 4 indicates the median Δv_{90} of the O VI systems in the catalog of C. W. Danforth et al. (2016). To obtain this information, we first used the Voigt profile fit parameters of all the O VI components in their catalog and defined systems using a linking velocity of 300 km s^{-1}. We excluded the systems in which one of the components had $\log_{10}(N(\mathrm{O\,VI})/\mathrm{cm}^{-2}) \geqslant 14$, as these strong absorbers are likely to be associated with the CGM of galaxies.[10] For each selected system, we generated a model absorption profile using the wavelength-dependent line-spread function of COS. Such model profiles are then used to determine the Δv_{90}.

The median Δv_{90} of $\approx$120 km s^{-1} from C. W. Danforth et al. (2016) is comparable to the median $\Delta v_{90} \approx 123$ km s^{-1} of the O VI systems associated with galaxies at $D < R_{\rm vir}$. However, the median $\Delta v_{90} \approx 227$ km s^{-1} for the group galaxies with $D < R_{\rm vir}$ is significantly higher than for the random regions. A two-sample KS test between the Δv_{90} distribution of group and isolated galaxies with $D < R_{\rm vir}$ results in a p-value of 0.06. This marginal difference is not present when galaxies at all impact parameters are considered ($p = 0.3$). The galaxies with $D \geqslant R_{\rm vir}$ have marginally lower median $\Delta v_{90} \approx 100$ km s^{-1}. Similar to the analysis of the b parameters, we find that the majority of the galaxies with narrow Δv_{90} at $D > R_{\rm vir}$ are not isolated.

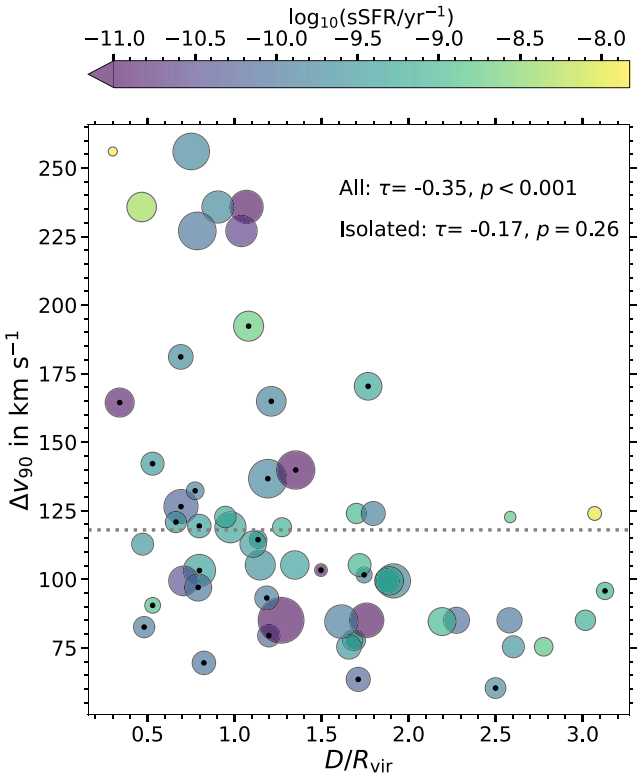

Figure 4. Δv_{90} of O VI absorption systems plotted against the $D/R_{\rm vir}$ of the associated galaxy. The points are color-coded by the sSFR of the galaxy. The galaxies with upper limits on sSFR are assigned a flag value of 10^{-11} yr^{-1}, where the color scale saturates. The area of the points is proportional to the stellar mass of the host galaxy. The absorption systems hosted by isolated galaxies are marked with black circles in the center. The horizontal gray dotted line indicates the median Δv_{90} constructed from the "galaxy-blind" O VI catalog of C. W. Danforth et al. (2016), considering only systems without any component with $\log_{10}(N(\mathrm{O\,VI})/\mathrm{cm}^{-2}) \geqslant 14$.

Further binning both the isolated and group subsamples based on stellar mass, we find a marginally higher $\Delta v_{90} \approx 140$ km s^{-1} for the massive ($\log_{10}(M_\star/M_\odot) \geqslant 9$) isolated galaxies compared to the low-mass ($\log_{10}(M_\star/M_\odot) < 9$) isolated galaxies $\Delta v_{90} \approx 100$ km s^{-1}. A significant difference in the median Δv_{90} between the low- and high-mass group galaxies ($\Delta v_{90} \approx 123$ and 230 km s^{-1}, respectively) is observed only when the impact parameter is $<R_{\rm vir}$. Δv_{90} is low for group galaxies at $D \geqslant R_{\rm vir}$ irrespective of the stellar mass.

Next, we used the pixel-velocity TPCF as an alternate method to characterize the velocity dispersion of O VI absorption systems (see, e.g., N. M. Nielsen et al. 2015). Briefly, the velocities of all spectral pixels within the full extent of the absorption system are compiled for a given subsample of galaxies, with a velocity of 0 km s^{-1} corresponding to the $z_{\rm sys}$ of the absorption system (see Section 2.2). The absolute velocity differences of all pixel pairs ($\boldsymbol{\Delta v}$) are calculated from this compilation before binning them into 20 km s^{-1} velocity

[10] Including these systems does not result in appreciable change of the median Δv_{90} of random regions.

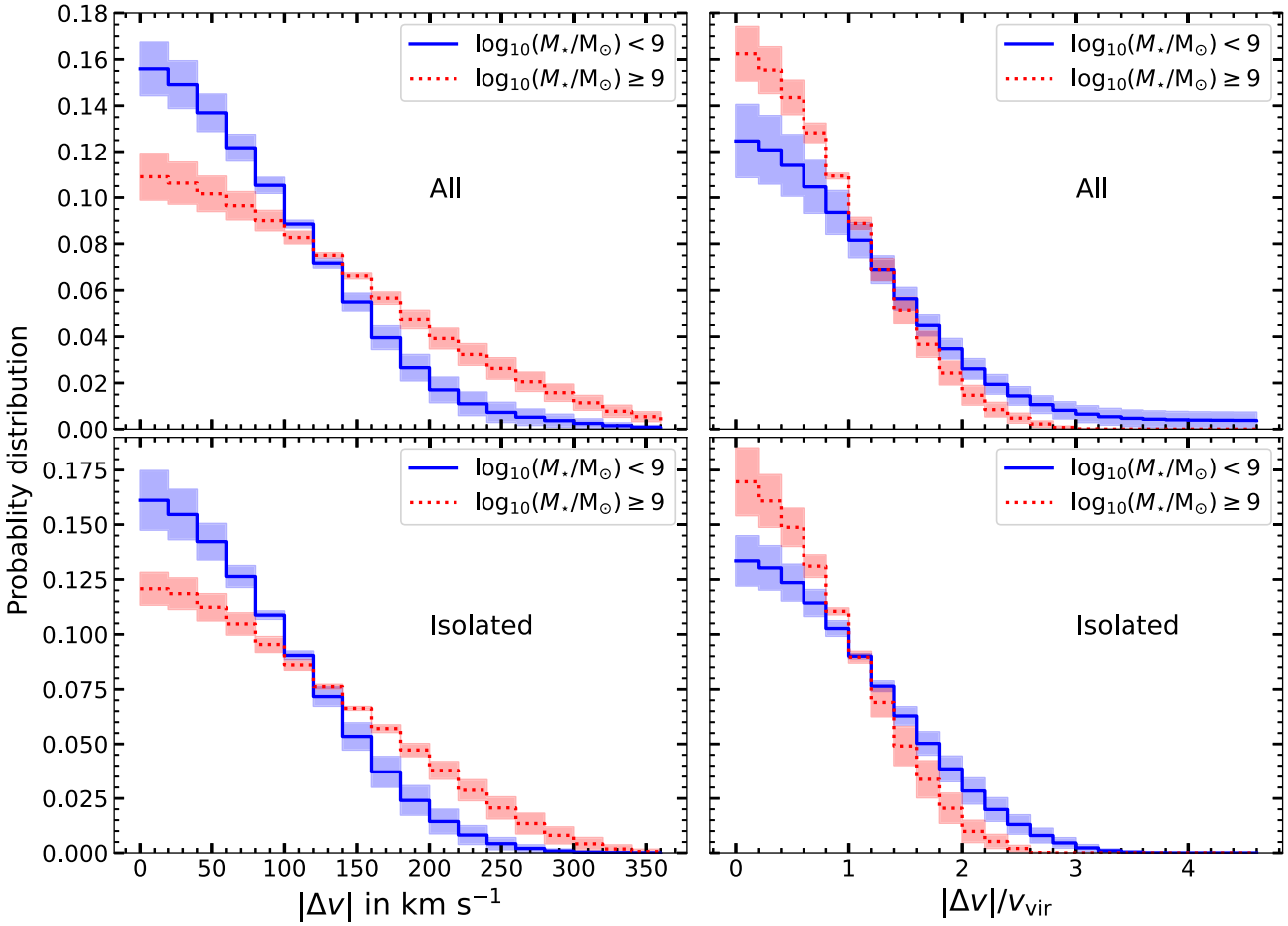

Figure 5. Comparison of the pixel-velocity TPCF for low-mass ($\log_{10}(M_\star/M_\odot) < 9$) and high-mass ($\log_{10}(M_\star/M_\odot) \geqslant 9$) bins, shown with solid blue and dotted red histograms, respectively, plotted against $|\Delta v|$ in the left panels and $|\Delta v|/v_{\rm vir}$ in the right panels. The top and bottom rows show the TPCF for the full sample and the isolated subsample, respectively.

windows. The count in each bin is then normalized by the total number of pairs in the subsample to obtain the probability distribution. We divide our MUSEQuBES galaxy sample with detected O VI absorption into two bins with $\log_{10}(M_\star/M_\odot) < 9$ and $\log_{10}(M_\star/M_\odot) \geqslant 9$. There are 33 and 27 galaxies in each respective bin. The O VI TPCFs for low- and high-mass bins are shown in the top left panel of Figure 5 with blue and red histograms, respectively. The shaded regions are the bootstrap errors obtained from 100 bootstrap realizations, with absolute velocity differences calculated from resampled pixel velocities. The O VI TPCF for the high-mass bin is significantly wider compared to its low-mass counterpart.

The larger velocity dispersion of O VI absorption in high-mass halos can arise from their higher circular velocities. In order to account for this difference, we produced a new O VI TPCF after scaling the absolute velocity differences of pixel pairs of an absorption system by the virial velocity ($\sqrt{GM_{\rm vir}/R_{\rm vir}}$) of the associated galaxy. The resulting scaled TPCFs for the low- and high-mass galaxies in the MUSE-QuBES sample are shown in the top right panel of Figure 5 with blue and red histograms, respectively. Interestingly, the scaled O VI TPCF reveals a reverse trend, with the low-mass galaxies showing marginally higher probabilities for velocities larger than the virial velocity. The profile for the high-mass galaxies, on the other hand, shows a sharp decline beyond the virial velocity. The excess probability at $|\Delta v|/v_{\rm vir} > 1$ for low-mass galaxies may be due to material efficiently escaping the halos with shallower gravitational potential wells.

However, another possible explanation for this excess probability is the presence of neighboring galaxies that share the same absorption system. To disentangle any potential role of the environment in the mass trend discussed above, we repeated the analysis using a subsample of only isolated galaxies. The O VI TPCF and normalized O VI TPCF for the isolated galaxies are shown in the bottom left and bottom right panels of Figure 5, respectively.

Consistent with the full sample, we observe a broader kinematic extent for the absorbers hosted by more massive galaxies (bottom left panel). This difference reduces for the normalized O VI TPCF (bottom right panel). However, the normalized O VI TPCF for both the complete sample and isolated subsample shows a marginal difference ($\approx 4.5\sigma$) between low- and high-mass galaxies, implying that the environment may not play a crucial role in the observed difference. The role of the environment in the kinematic extent of O VI absorption is further discussed in Section 4.3.

4. Discussion

We have studied the connection between galaxy properties and the kinematics of O VI absorption in the CGM of low-redshift (0.1−0.7) galaxies.

In this section, we discuss the main findings from Section 3.

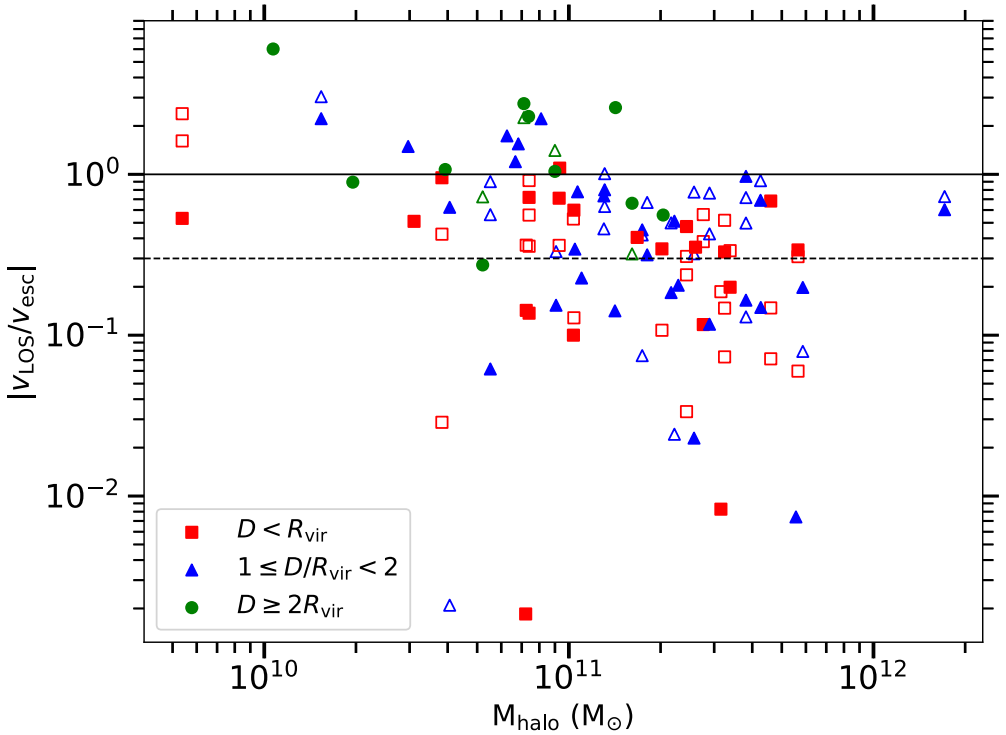

Figure 6. The velocity of O VI components (v_{LOS}) scaled by local escape velocity [$v_{esc}(D)$] is plotted against the halo mass of the associated galaxy for the MUSEQuBES sample with red squares (for galaxies with $D < R_{vir}$), blue triangles ($1 \leqslant D/R_{vir} < 2$), and green circles ($D \geqslant 2R_{vir}$). The filled and open symbols represent the primary (strongest) and secondary components of an absorption system, respectively. The horizontal lines indicate $|v_{LOS}/v_{esc}(D)| = 1$ (solid) and $|v_{LOS}/v_{esc}(D)| = 1/\sqrt{3}$ (dashed) (the latter accounts for the projection effect).

4.1. Are the O VI Components Bound to the Dwarf Galaxies?

The velocity distribution of O VI absorption components around MUSEQuBES galaxies shows significant clustering within ± 86 km s^{-1} (Figure 2). The velocity scale of clustering is larger[11] than the projected virial velocity of ≈ 46 km s^{-1} for galaxies with the median $\log_{10}(M_\star/M_\odot) = 8.9$ in our MUSEQuBES sample for which O VI absorption is detected. Here we investigate how the LOS velocities compare with respect to the local escape velocities of the halos.

In Figure 6, we show the absolute LOS velocity of individual O VI components with respect to the host galaxy redshift, normalized by the local escape velocity[12] ($|v_{LOS}/v_{esc}(D)|$), plotted against the halo mass with red squares (for galaxies with $D < R_{vir}$), blue triangles (for galaxies with $1 \leqslant D/R_{vir} < 2$), and green circles (for galaxies with $D \geqslant 2R_{vir}$) for the galaxies in our sample. The filled and open symbols represent the primary (strongest) and secondary (weaker) components of an absorption system, respectively. The horizontal solid line represents $|v_{LOS}/v_{esc}(D)| = 1$. The horizontal dashed line represents $|v_{LOS}/v_{esc}| = 1/\sqrt{3}$, which accounts for the projection effects on the LOS velocity.

We determine the "bound fraction" defined as $n_1/(n_1 + n_2)$, where n_1 and n_2 are the number of components with $|v_{LOS}/v_{esc}(D)| \leqslant 1$ and > 1, respectively. However, we note that this number relies on quantities with large uncertainties (such as M_{halo}). Additionally, the impact parameter D represents the *minimum* possible 3D distance of the absorbers, and v_{LOS} is a lower limit on the 3D velocity. Hence, this is an upper limit on the fraction of truly bound absorbers. The bound fractions for different halo mass and impact parameter bins are tabulated in Table 1. The bound fraction is <83% for the full MUSEQuBES sample, which reduces to <62% when the $|v_{LOS}/v_{esc}(D)| \leqslant 1/\sqrt{3}$ is considered to be bound. This indicates that, overall, a considerable fraction of the O VI components in our sample may not be bound to the host halo. However, consistent with previous surveys, we obtain a bound fraction (upper limit) of unity for halos with $M_{halo} > 10^{11.5}\ M_\odot$ out to $\approx 2R_{vir}$ (J. Tumlinson et al. 2011; N. L. Mathes et al. 2014). For the low-mass halos with $M_{halo} \leqslant 10^{11.5}\ M_\odot$, the bound fraction is <91% within R_{vir}, which decreases to <79% between $1R_{vir}$ and $2R_{vir}$ and further decreases to <43% at $>2R_{vir}$. We thus conclude that O VI absorbers detected within R_{vir} are likely predominately bound to the host halos, even for

Table 1
Summary of O VI Bound Fraction Measurements

$\log_{10}(M_{halo}/M_\odot)$	Upper Limit on the Bound Fraction at Different D/R_{vir}			
	All	$D < R_{vir}$	$1 \leqslant D/R_{vir} < 2$	$D \geqslant 2R_{vir}$
All	0.83 (0.62)	0.94 (0.81)	0.85 (0.56)	0.43 (0.21)
$\leqslant$11.5	0.78 (0.59)	0.91 (0.77)	0.79 (0.56)	0.43 (0.21)
>11.5	1.0 (0.72)	1.0 (0.92)	1.0 (0.54)	...

Notes. There are no galaxies with $\log_{10}(M_{halo}/M_\odot) > 11.5$ at $D \geqslant 2R_{vir}$. The bound fraction with respect to the projected escape velocity ($v_{esc}(D)/\sqrt{3}$) is indicated in parentheses.

[11] Even when the redshift uncertainties of ≈ 40 km s^{-1} are considered.

[12] We assumed a Navarro–Frenk–White density profile for the host halo mass, with local escape velocity at a given distance D given by $v_{esc}(D) = \sqrt{(2GM_{halo}/D)\ln[1 + c(D/R_{vir})]/[\ln(1 + c) - c/(1 + c)]}$. The halo-mass- and redshift-dependent concentration parameter c is obtained using the COMMAH package (C. A. Correa et al. 2015).

dwarf galaxies. We verified that the results are consistent if we use $3v_{\rm esc}(D)$ or $6v_{\rm esc}(D)$ for galaxy–absorber association instead of a fixed LOS window of $\pm300\,{\rm km\,s^{-1}}$ used here. A high bound fraction of $\lesssim$83% for O VI absorbers in isolated dwarf galaxies (median $\log_{10}(M_\star/M_\odot) \approx 8.4$) at $D/R_{\rm vir} \lesssim 2$ was recently observed in the CUBS survey (N. Mishra et al. 2024). This is fully consistent with our findings (see Table 1).

Based on a small sample of 14 galaxies, N. L. Mathes et al. (2014) reported that galaxies with halo mass $<10^{11.5}\,M_\odot$ have a bound fraction of only $<$0.50, in contrast to the $<$0.91 we measured here. This is likely because their O VI measurements for low-mass galaxies are small in number and the majority of them have $D > R_{\rm vir}$ (7/8). The one O VI component associated with a low-mass galaxy at $D < R_{\rm vir}$ is consistent with being bound to the host galaxy, in agreement with our findings. By comparing the O VI kinematics with the radial velocities of a simulated galaxy ($M_{\rm halo} \approx 2 \times 10^{11}\,M_\odot$), the authors argued that the absorbing clouds with $|v_{\rm LOS}/v_{\rm esc}(D)| > 1$ are likely to be outflowing winds since infalling gas does not exceed the escape velocity. Indeed, there is observational evidence that star-formation-driven outflows from dwarf galaxies can have velocities larger than the escape velocity (see, e.g., M. Romano et al. 2023). The ≈20% of the O VI components detected at $D > R_{\rm vir}$ in low-mass halos that exceed the escape velocities in our sample may indicate that they stem from outflows. Alternatively, the two-halo contributions, which become important at larger $D/R_{\rm vir}$, can give rise to LOS velocities exceeding the escape velocity for low-mass galaxies (see S. H. Ho et al. 2021).

4.2. Turbulence in the O VI-bearing Circumgalactic Gas

Feedback due to AGN- and supernova-driven winds and mergers can inject significant turbulence into the CGM, in addition to enriching it with metals. It is therefore important to obtain direct constraints on the turbulence in the CGM. In Section 3.2, we reported that a substantial fraction of O VI components require high turbulent velocity ($b_{\rm turb} \geqslant 20\,{\rm km\,s^{-1}}$) to explain their observed b parameters, assuming that the maximum attainable gas temperature is equal to the virial temperature (see Figure 3). Decomposing the b parameters into thermal and turbulent components and assuming that the thermal broadening is due to the virial temperature of the host halo, we obtain a range of $b_{\rm turb} \approx$ 5–60 km s^{-1} with a median of 22 km s^{-1} and a mean of 25 km s^{-1}. J. K. Werk et al. (2016) reported an average $b_{\rm turb}$ of ≈40–50 km s^{-1} for the O VI absorbers in the COS-Halos sample, assuming that the thermal broadening ranges from 6.4 to 16.2 km s^{-1}. Our inferred $b_{\rm turb}$ values are marginally lower than those of J. K. Werk et al. (2016). Recently, H.-W. Chen et al. (2023) reported $b_{\rm turb}$ of ≈5–30 km s^{-1} for a sample of well-aligned H I and low-ionization metal lines in the CGM of low-z galaxies. J. K. Werk et al. (2016) also inferred $b_{\rm turb} < 20\,{\rm km\,s^{-1}}$ for the Si III (low-ionization) line. This may suggest that the different phases of the CGM are subject to different turbulent motions.

Several galaxy-blind absorption-line studies used aligned H I–O VI absorption pairs to solve for the thermal and nonthermal components of the b parameter at both low z (e.g., T. M. Tripp et al. 2008; B. D. Savage et al. 2014) and high z (i.e., S. Muzahid et al. 2012). While the gas temperature turned out to be similar at low and high redshifts for the well-aligned H I–O VI pairs, the median $b_{\rm turb}$ was found to be 2–3 times larger at low z (i.e., 20–30 km s^{-1}). The median $b_{\rm turb}$ values obtained from blind absorption-line studies are somewhat smaller than our inferred values but are consistent with the predictions of the theoretical models of C. Evoli & A. Ferrara (2011).

Recently, based on both small-scale and large-scale simulations, B. Koplitz et al. (2023) argued that $\sigma_{\rm LOS}$, defined as the standard deviation of velocity centroids of components along a sight line, is a better indicator of true LOS turbulence than $b_{\rm turb}$, as it can capture the intercloud motions along with the random motions within individual clouds. Since most of our O VI absorbers are composed of one or two components, Δv_{90} is a good proxy for the $\sigma_{\rm LOS}$. The moderate anticorrelation of Δv_{90} with $D/R_{\rm vir}$ observed in this work (see Figure 4) may indicate decreasing turbulence in the outer CGM. This is in agreement with the observed anticorrelation between velocity dispersion of O VI absorbers and $D/R_{\rm vir}$ in Z. Qu et al. (2024). S. Borthakur et al. (2016), on the contrary, found an increasing trend in $\sigma_{\rm LOS}$, quantified as $b/\sqrt{2}$ of the strongest component, with $D/R_{\rm vir}$ based on their H I measurements. We observe a moderate anticorrelation of b with $D/R_{\rm vir}$ for our O VI sample (see right panel of Figure 3). We verified that selecting only the strongest component associated with the host galaxy does not change our results. Here we note that the galaxies in the S. Borthakur et al. (2016) sample extend to a higher halo mass range ($\log_{10}(M_{\rm halo}/M_\odot) \approx 11.5 - 13$) as compared to our sample ($\log_{10}(M_{\rm halo}/M_\odot) \approx 10 - 12$). Additionally, different phases traced by H I and O VI may give rise to this apparent contrast in the turbulent velocity in the CGM.

4.3. The Connection between O VI Kinematics and Galaxy Environment

In Section 3.3 we showed that the overall kinematic extent of circumgalactic O VI absorbers, characterized by the TPCF, is wider for high-mass galaxies. This is consistent with the findings of M. Ng et al. (2019). The difference reduces (≈4.5σ) when the normalized O VI TPCF is considered, with the low-mass subsample showing marginally higher probabilities at $|\Delta v| > v_{\rm vir}$ compared to the high-mass subsample. Selecting the isolated subsample results in a consistent picture, hinting at a negligible role in the environment on the kinematic extent of O VI absorptions. Here we investigate the effect of "group" galaxies on the kinematic extent of the O VI absorption.

The FoF algorithm used to identify isolated galaxies also provides us with a subsample of galaxies with one or more neighbors within $\pm500\,{\rm km\,s^{-1}}$ of one another and a maximum projected distance of ≈500 kpc. We refer to this as our "group" subsample. The left panel of Figure 7 shows the TPCFs of O VI absorption for the group galaxies with group-occupation number (GOcc) $\leqslant 3$ and $\geqslant 4$ with dotted purple and dashed green lines, respectively. The shaded regions represent 68% confidence intervals obtained with 100 bootstrap realizations. Note that we use an absorption system associated with a group only once in this exercise. The O VI TPCF, shown with a solid black line, is for isolated galaxies with stellar mass matched to the galaxies in the GOcc $\leqslant 3$ group (median $\log_{10}(M_\star/M_\odot) \approx 8.8$). It is intriguing to note that the O VI TPCF for the densest group (GOcc $\geqslant 4$), despite the higher median stellar mass of the member galaxies (median $\log_{10}(M_\star/M_\odot) \approx 9.3$), is significantly narrower compared to the other two subsamples. The difference between the mass-controlled isolated galaxies and GOcc $\leqslant 3$ group galaxies is not that prominent. The

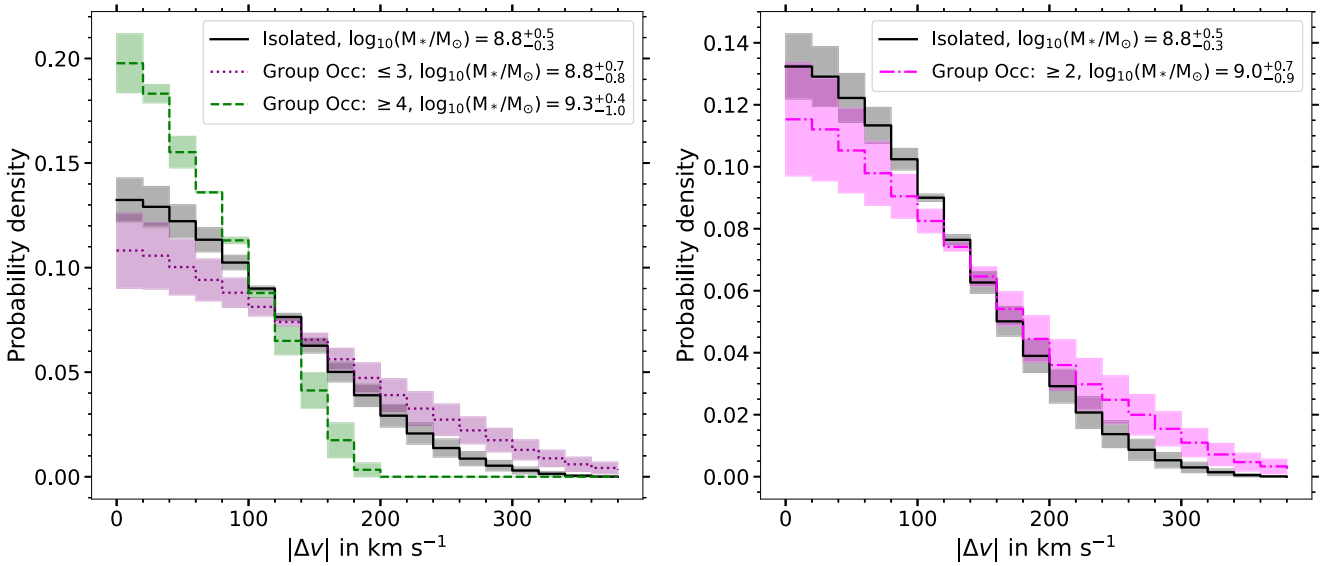

Figure 7. Left: TPCFs of O VI absorption for isolated galaxies and group galaxies with occupancy GOcc $\leqslant 3$ and $\geqslant 4$ shown with solid black, dotted purple, and dashed green lines, respectively. There are nine and two groups with GOcc $\leqslant 3$ and $\geqslant 4$, respectively, hosting O VI absorption. The shaded regions represent 68% confidence intervals obtained with 100 bootstrap realizations. The stellar mass of the isolated sample is matched to the galaxies in the GOcc $\leqslant 3$ group. The TPCF for the GOcc $\geqslant 4$ group is significantly narrower compared to the rest. Right: TPCF of O VI absorption for the group galaxies following the definition of S. K. Pointon et al. (2017), shown with the magenta dashed–dotted line. The TPCF for the isolated galaxies is the same as in the left panel. No significant difference is seen in the TPCFs of O VI absorption for the two samples. The median stellar mass of the contributing galaxies is indicated in the legends, with subscripts and superscripts representing the 68% range.

GOcc $\leqslant 3$ group shows a somewhat wider O VI TPCF compared to the isolated subsample.

By comparing the O VI TPCFs of isolated and group galaxies, S. K. Pointon et al. (2017) reported that the velocity spread of O VI in the CGM of group galaxies is significantly (10σ) narrower than that of isolated galaxies.[13] They suggested that the gas traced by O VI in group galaxies is located at the interface of warm CGM of individual group galaxies and the hotter region of the intragroup medium at the virial temperature. The narrow profiles are, according to them, a consequence of low column density gas in the higher-velocity wings being further ionized owing to higher temperature. We see such a stark difference only for the GOcc $\geqslant 4$ group sample. Out of the six groups that show detectable O VI absorption in the sample of S. K. Pointon et al. (2017), only one has GOcc $\geqslant 4$. If we adopt a group definition similar to that of S. K. Pointon et al. (2017), we find *a marginal* 2σ difference between the O VI TPCFs of isolated and group subsamples, with a somewhat broader kinematic profile for the group galaxies (see the right panel of Figure 7). Since we observed a strong mass dependence for the O VI TPCF (bottom left panel of Figure 5), this marginal difference can be attributed to the slightly higher median mass for the group galaxies. It is therefore important to control for the stellar mass, particularly when the O VI TPCF is not normalized by the circular velocity.

It is worthwhile to note that a significant fraction of groups with large occupation numbers (GOcc $\geqslant 4$) do not show any detectable O VI absorption. Out of the six groups with GOcc $\geqslant 4$, only two show detectable O VI absorption, totaling three Voigt profile components with b parameters of 11.2 ± 2.9 km s^{-1}, 15.0 ± 2.4 km s^{-1}, and 36.7 ± 4.9 km s^{-1}. None of these components are consistent with temperatures $\geqslant 10^{5.5}$ K when compared[14] with the b value of the nearest H I component. In fact, the inferred gas temperature for these three components (i.e., a few $\times$ 10^4 K) is similar to what is expected from photoionized gas. Evidently, the narrowness of the O VI TPCF for the GOcc $\geqslant 4$ group is not because of the gas being overheated. Nevertheless, the nondetection of O VI for a significant fraction of groups with GOcc $\geqslant 4$ (i.e., $\approx$67% for our sample and $\approx$50% for S. K. Pointon et al. 2017) is intriguing. This could be an indication that the medium is too hot for O VI.

To further investigate the nondetection of O VI in four of six GOcc $\geqslant 4$ groups in our sample, we found that in every group there is at least one member galaxy with an impact parameter $<R_{\rm vir}$. In fact, there are a total of 11 member galaxies in those four groups with $D < R_{\rm vir}$. However, only 2 of 11 galaxies are classified as "SF." Thus, the lack of O VI in these groups can also be attributed to the lower O VI covering fraction in the CGM of passive galaxies, as shown in Paper I (see also B. D. Oppenheimer et al. 2016; K. Tchernyshyov et al. 2022). On the contrary, one of the two groups with detected O VI absorption has no galaxy within $R_{\rm vir}$. In the other group with detected O VI, the nearest $D/R_{\rm vir}$ galaxy is a star-forming galaxy. However, in terms of the total stellar mass of galaxies in the groups (or the mass of the most massive galaxy of the group), we do not observe any significant difference between the groups with and without O VI absorption.

5. Summary

In this paper, we present a study of the kinematics of O VI-bearing gas around 60 low-redshift ($0.1 \lesssim z \lesssim 0.7$) galaxies with a median [68% range] $\log_{10}(M_\star/M_\odot) = 8.9$ [8.1–9.7] and median [68% range] $D = 115$ kpc [64–192 kpc] observed in 16 quasar fields in MUSEQuBES. The O VI absorption systems

[13] They defined a galaxy group as two or more galaxies with an LOS velocity difference of no more than 1000 km s^{-1} and located within 350 kpc (projected) of a background quasar sight line.

[14] We decompose the b parameter into thermal and nonthermal components using b(O VI) and b(H I).

detected around these galaxies enabled us to investigate the connections between galaxy properties on the O VI kinematics. Our key findings are as follows:

1. We found that ≈83% of all the O VI components detected within $\pm 300\,\mathrm{km\,s^{-1}}$ of the galaxy redshifts have $v_{\rm LOS}/v_{\rm esc}(D) < 1$. The fraction increases to 94% when only galaxies with $D < R_{\rm vir}$ are considered. Even for dwarf galaxies ($\log_{10}(M_\star/\mathrm{M}_\odot) < 9$), ≈91% of the O VI components detected within $R_{\rm vir}$ are consistent with being bound to the host halo (Table 1).
2. The b parameter of the O VI components and the Δv_{90} of the O VI systems associated with the galaxies show a mild anticorrelation with $D/R_{\rm vir}$. Significantly larger b and Δv_{90} values, compared to galaxy-blind O VI absorbers, are seen at $D \lesssim 1.5R_{\rm vir}$ (Figures 3 and 4).
3. A positive trend is observed between the b parameter and $M_\star$ for the isolated galaxies ($\tau = 0.25$, $p = 0.02$; Figure 3). Assuming that the thermal broadening is due to the virial temperature of the host halo, we determine nonthermal broadening to be in the range 5–60 $\mathrm{km\,s^{-1}}$, with a median of 22 $\mathrm{km\,s^{-1}}$.
4. The velocity TPCF of O VI absorption for the high-mass galaxies ($\log_{10}(M_\star/M_\odot) > 9$) is significantly broader compared to their low-mass counterpart. However, the difference becomes marginal when the TPCF is normalized by the circular velocity (Figure 5). We do not find any significant difference between the TPCF of isolated and group (with GOcc $\geqslant 2$) subsamples when the stellar mass is matched (Figure 7, right panel).
5. The O VI TPCF of the group subsample with GOcc $\geqslant 4$ is significantly narrower compared to the isolated subsample and group subsample with GOcc $\leqslant 3$ (Figure 7, left panel). The observed b parameters of the two O VI systems contributing to the TPCF indicate that the narrowness of the TPCF is *not* due to high gas temperatures. However, we note that four of six groups with GOcc $\geqslant 4$ do not exhibit any detectable O VI absorption, which may be an indication that the medium is too hot for O VI. The prevalence of passive galaxies in such galaxy overdensity can also explain the lack of O VI detection. As such, we do not find any convincing evidence that the O VI kinematics depend on the galaxy environment.

Acknowledgments

We sincerely thank the anonymous referee for detailed and constructive feedback on the manuscript. S.D. and S.M. acknowledge support from the Indo-Italian Executive Programme of Scientific and Technological Cooperation 2022–2024 (TPN: 63673). S.D. acknowledges Prof. R. Srianand and Dr. Aseem Paranjape for insightful discussions.

Appendix A
Galaxy–Absorber Connection: Unique Host

Selecting the galaxy with minimum D, minimum $D/R_{\rm vir}$, or maximum $M_\star$ within a group to associate with the O VI systems results in unique galaxy–absorber pairs, with each absorber associated with one and only one host galaxy. In Figures 8, 9, and 10, we show that, even with the unique galaxy–absorber pairs, our main conclusions from Figures 3, 4, and 5 remain unchanged.

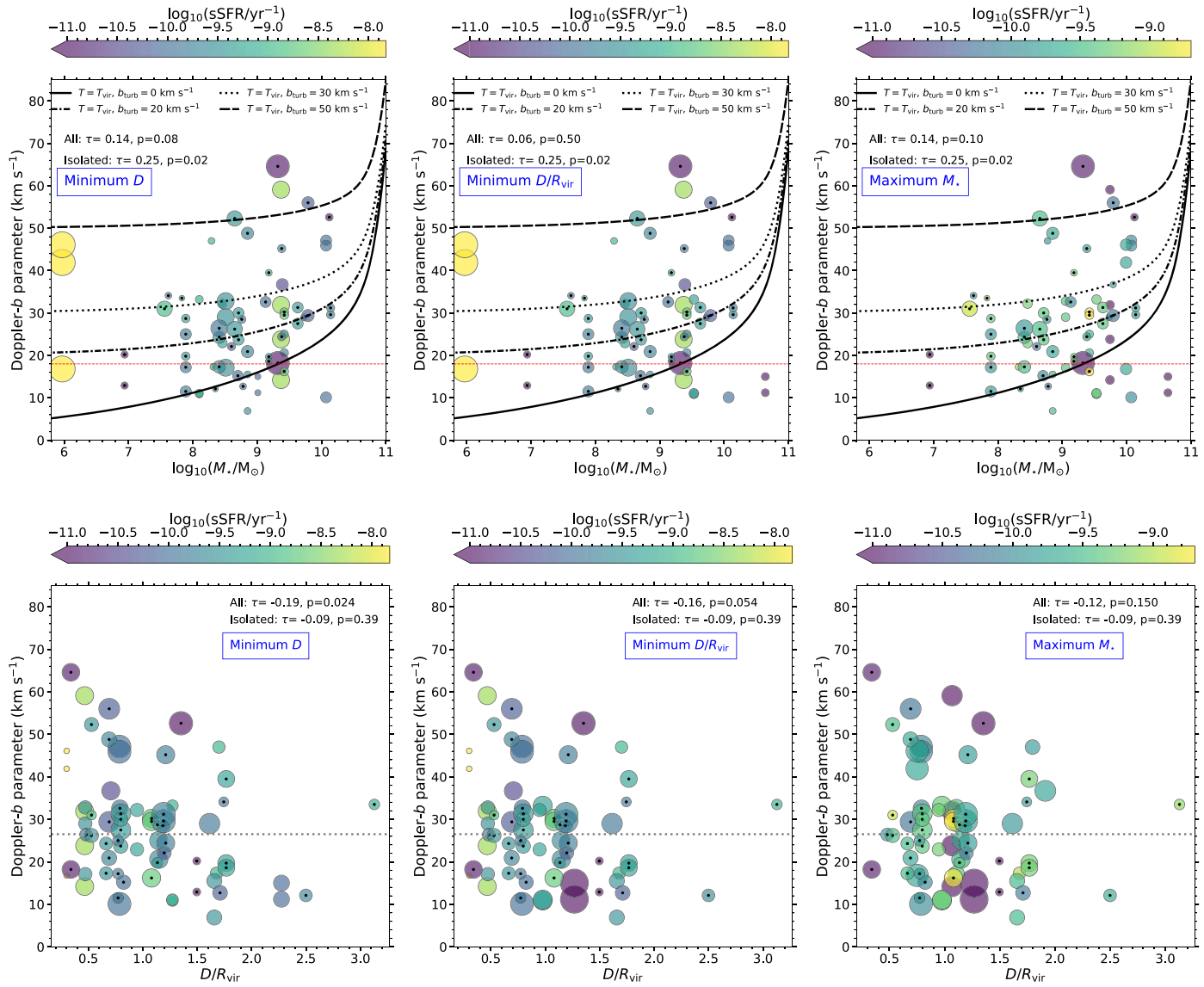

Figure 8. Top and bottom panels are same as the left and right panels of Figure 3, but O VI components are assigned to only one host galaxy based on the minimum D, minimum $D/R_{\rm vir}$, or maximum $M_\star$ from left to right.

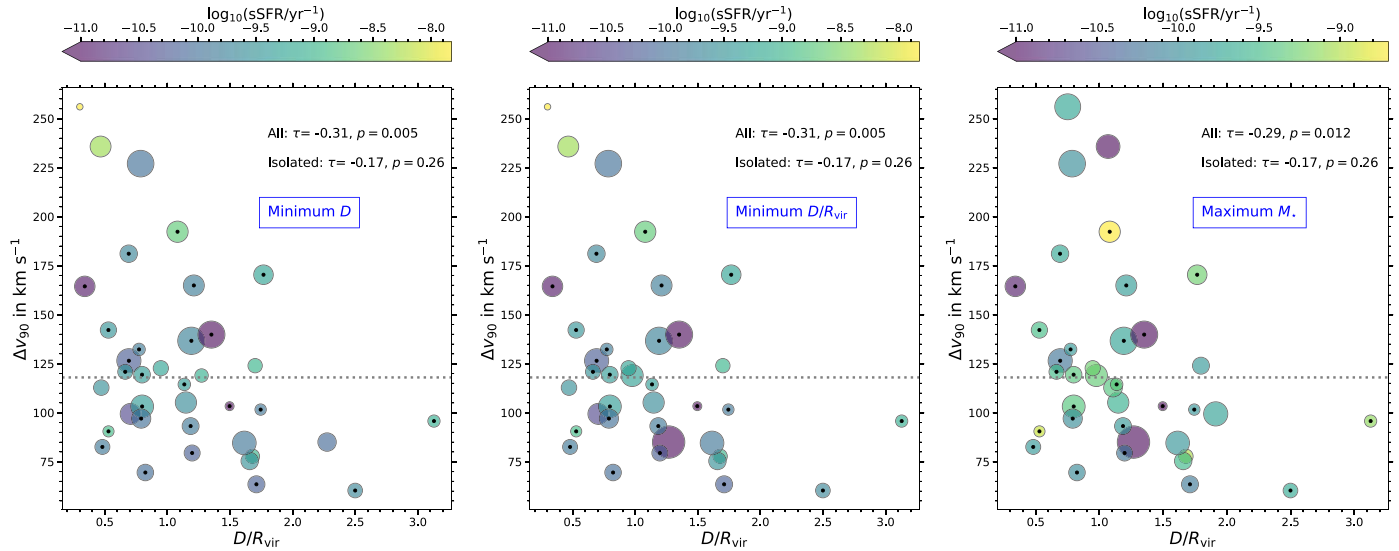

Figure 9. Same as Figure 4, but O VI components are assigned to only one host galaxy based on the minimum D, minimum $D/R_{\rm vir}$, or maximum $M_\star$ from left to right.

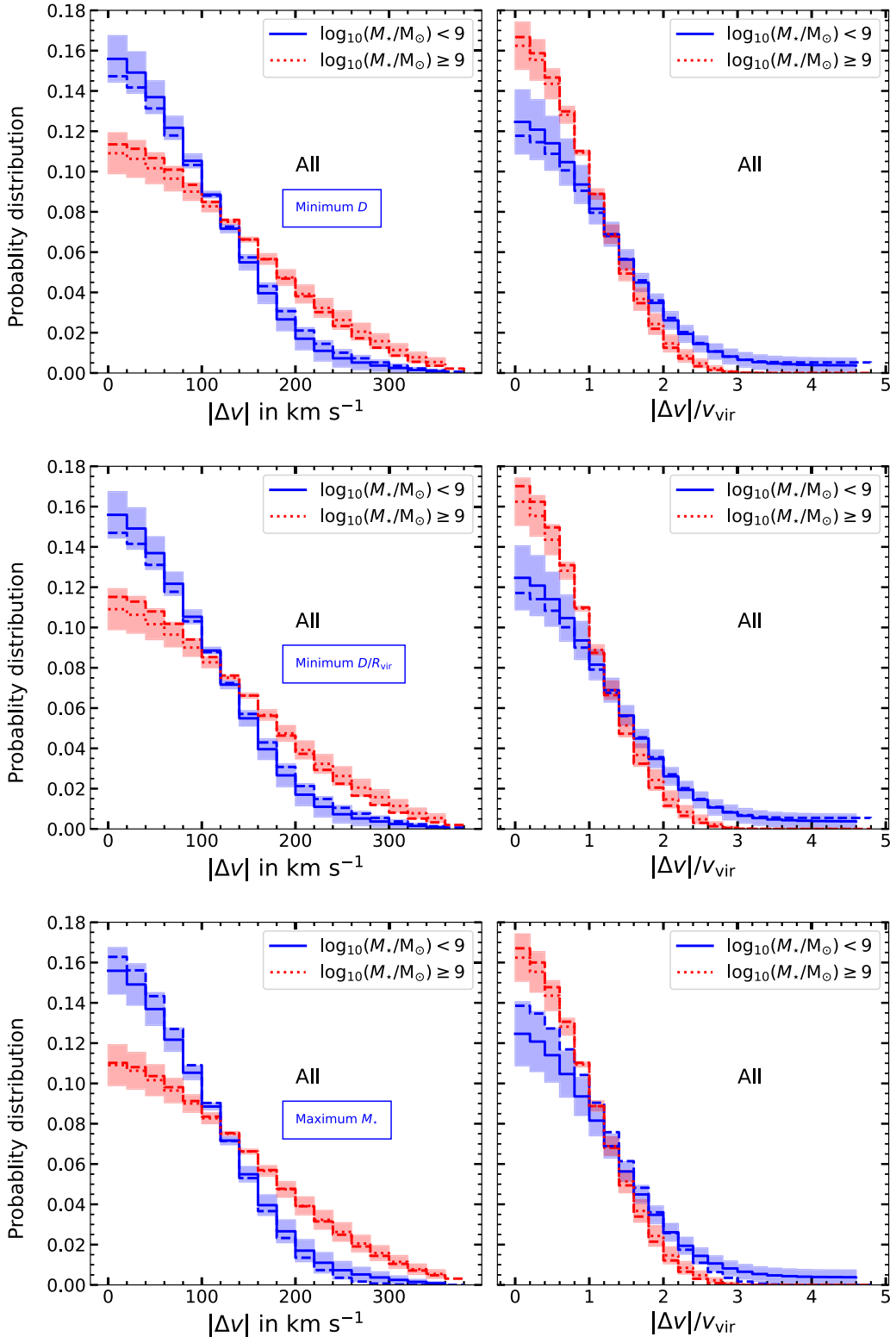

Figure 10. Same as the top rows in Figure 5. The dashed blue and dashed red histograms represent O VI TPCF when O VI systems are assigned to only one host galaxy (based on the minimum D, minimum D/R_{vir}, or maximum $M_\star$, from top to bottom).

Appendix B
Online-only Tables

Here we present the galaxy and associated absorption component properties for the 60 galaxies with detected O VI absorption (Tables 2 and 3).

Table 2
Galaxy–O VI Component Pairs

GalId	$\log_{10}(M_\star/M_\odot)$	D (kpc)	b (km s^{-1})	$z_{\rm gal}$	$z_{\rm comp}$
1	8.41	36.78	26.4	0.3333	0.3333
2	8.65	44.19	26.2	0.3249	0.3247
2	8.65	44.19	52.3	0.3249	0.3244
3	9.79	88.86	29.4	0.3284	0.3282
3	9.79	88.86	56.0	0.3284	0.3281
4	8.41	50.22	17.3	0.3835	0.3837
4	8.41	50.22	24.3	0.3835	0.3834
5	8.7	70.88	15.2	0.2496	0.2502
6	8.35	178.42	12.1	0.5322	0.5333
7	10.14	176.53	29.6	0.4318	0.4316
7	10.14	176.53	31.2	0.4318	0.4319
8	8.78	149.83	12.7	0.3227	0.3231
9	7.62	103.34	34.1	0.2256	0.226
10	7.89	72.89	19.8	0.2909	0.2912
10	7.89	72.89	28.7	0.2909	0.2909
11	8.71	67.1	23.7	0.4002	0.4006
11	8.71	67.1	30.0	0.4002	0.4003
12	9.38	130.22	24.4	0.4243	0.4243
12	9.38	130.22	45.2	0.4243	0.4239
13	8.29	125.33	47.0	0.3089	0.3083
14	7.56	27.86	31.0	0.5723	0.5726
15	9.74	127.52	14.2	0.6158	0.615
15	9.74	127.52	23.8	0.6158	0.6153
15	9.74	127.52	31.9	0.6158	0.6147
15	9.74	127.52	59.1	0.6158	0.6157
16	9.61	102.36	14.2	0.6151	0.615
16	9.61	102.36	23.8	0.6151	0.6153
16	9.61	102.36	31.9	0.6151	0.6147
16	9.61	102.36	59.1	0.6151	0.6157
17	9.37	47.93	14.2	0.6153	0.615
17	9.37	47.93	23.8	0.6153	0.6153
17	9.37	47.93	31.9	0.6153	0.6147
17	9.37	47.93	59.1	0.6153	0.6157
18	7.19	153.39	47.0	0.3085	0.3083
19	8.77	157.19	47.0	0.3081	0.3083
20	8.3	122.32	17.3	0.4179	0.4185
21	8.32	122.03	17.3	0.4192	0.4185
22	9.63	93.04	27.5	0.5172	0.5172
22	9.63	93.04	31.3	0.5172	0.517
23	9.39	71.38	36.7	0.7175	0.7179
24	8.6	100.0	22.1	0.2021	0.2031
25	9.28	182.6	36.7	0.7181	0.7179
26	10.12	199.31	52.6	0.3992	0.3992
27	9.79	227.65	36.7	0.7177	0.7179
28	8.87	154.63	36.7	0.7178	0.7179
29	9.53	109.82	10.9	0.4949	0.4953
29	9.53	109.82	11.1	0.4949	0.4955
29	9.53	109.82	33.2	0.4949	0.495
30	8.1	83.72	10.9	0.495	0.4953
30	8.1	83.72	11.1	0.495	0.4955
30	8.1	83.72	33.2	0.495	0.495
31	7.89	50.66	11.5	0.1825	0.1826
31	7.89	50.66	17.2	0.1825	0.1829
31	7.89	50.66	25.0	0.1825	0.1827
32	7.83	193.48	33.5	0.3612	0.3615
33	9.82	216.4	11.2	0.6326	0.6316
33	9.82	216.4	15.0	0.6326	0.6319
34	10.64	247.94	11.2	0.633	0.6316
34	10.64	247.94	15.0	0.633	0.6319
35	8.9	220.19	15.0	0.6335	0.6319
36	9.01	202.62	11.2	0.6314	0.6316
36	9.01	202.62	15.0	0.6314	0.6319

Table 2
(Continued)

GalId	$\log_{10}(M_\star/M_\odot)$	D (kpc)	b (km s^{-1})	$z_{\rm gal}$	$z_{\rm comp}$
37	8.29	204.59	11.2	0.6306	0.6316
37	8.29	204.59	15.0	0.6306	0.6319
38	6.94	65.51	12.9	0.4468	0.4459
38	6.94	65.51	20.2	0.4468	0.4461
39	9.32	35.97	18.2	0.3845	0.3846
39	9.32	35.97	64.6	0.3845	0.3849
40	9.55	116.91	10.1	0.5358	0.5365
40	9.55	116.91	45.9	0.5358	0.5362
40	9.55	116.91	47.1	0.5358	0.5357
41	10.07	110.43	10.1	0.5361	0.5365
41	10.07	110.43	45.9	0.5361	0.5362
41	10.07	110.43	47.1	0.5361	0.5357
42	9.13	77.23	32.6	0.4297	0.43
43	8.52	196.43	6.9	0.5582	0.5576
43	8.52	196.43	15.5	0.5582	0.5575
44	8.03	174.72	6.9	0.5578	0.5576
44	8.03	174.72	15.5	0.5578	0.5575
45	9.18	176.94	18.6	0.3993	0.3992

Table 3
Galaxy–O VI Component Pairs (Continued)

GalId	$\log_{10}(M_\star/M_\odot)$	D (kpc)	b (km s$^{-1)}$	$z_{\rm gal}$	$z_{\rm comp}$
45	9.18	176.94	19.7	0.3993	0.399
45	9.18	176.94	39.5	0.3993	0.3996
46	8.85	141.62	6.9	0.5572	0.5576
46	8.85	141.62	15.5	0.5572	0.5575
47	9.42	113.46	16.2	0.6103	0.61
47	9.42	113.46	29.5	0.6103	0.6103
47	9.42	113.46	30.2	0.6103	0.6095
48	9.21	210.47	29.0	0.6401	0.6405
49	9.73	190.83	29.0	0.6407	0.6405
50	9.42	127.32	20.6	0.3215	0.3216
50	9.42	127.32	25.0	0.3215	0.3219
51	9.26	140.59	20.6	0.3214	0.3216
51	9.26	140.59	25.0	0.3214	0.3219
52	8.85	63.07	20.9	0.184	0.1837
52	8.85	63.07	48.8	0.184	0.1841
53	8.76	101.31	28.5	0.4129	0.4128
54	8.63	142.64	20.6	0.3217	0.3216
54	8.63	142.64	25.0	0.3217	0.3219
55	6.63	107.96	22.9	0.2502	0.2512
56	8.46	74.87	22.9	0.2514	0.2512
56	8.46	74.87	32.2	0.2514	0.2515
57	9.05	108.3	17.1	0.2066	0.207
57	9.05	108.3	29.0	0.2066	0.2072
57	9.05	108.3	32.8	0.2066	0.2069
58	8.51	38.16	17.1	0.2066	0.207
58	8.51	38.16	29.0	0.2066	0.2072
58	8.51	38.16	32.8	0.2066	0.2069
59	5.97	9.47	16.8	0.3904	0.3896
59	5.97	9.47	41.9	0.3904	0.3899
59	5.97	9.47	46.1	0.3904	0.3906
60	9.99	104.35	16.8	0.3898	0.3896
60	9.99	104.35	41.9	0.3898	0.3899
60	9.99	104.35	46.1	0.3898	0.3906

ORCID iDs

Sayak Dutta https://orcid.org/0009-0000-0797-7365
Sowgat Muzahid https://orcid.org/0000-0003-3938-8762
Joop Schaye https://orcid.org/0000-0002-0668-5560
Sebastiano Cantalupo https://orcid.org/0000-0001-5804-1428
Hsiao-Wen Chen https://orcid.org/0000-0001-8813-4182
Sean Johnson https://orcid.org/0000-0001-9487-8583

References

Bacon, R., Accardo, M., Adjali, L., et al. 2010, Proc. SPIE, 7735, 773508
Banerjee, E., Muzahid, S., Schaye, J., Johnson, S. D., & Cantalupo, S. 2023, MNRAS, 524, 5148
Bergeron, J., & Stasińska, G. 1986, A&A, 169, 1
Boogaard, L. A., Brinchmann, J., Bouché, N., et al. 2018, A&A, 619, A27
Borthakur, S., Heckman, T., Tumlinson, J., et al. 2016, ApJ, 833, 259
Bouché, N., Murphy, M. T., Kacprzak, G. G., et al. 2013, Sci, 341, 50
Carswell, R. F., & Webb, J. K., 2014 VPFIT: Voigt Profile Fitting Program, Astrophysics Source Code Library, ascl:1408.015
Chabrier, G. 2003, ApJL, 586, L133
Chen, H.-W., Qu, Z., Rauch, M., et al. 2023, ApJL, 955, L25
Correa, C. A., Wyithe, J. S. B., Schaye, J., & Duffy, A. R. 2015, MNRAS, 452, 1217
Danforth, C. W., Keeney, B. A., Tilton, E. M., et al. 2016, ApJ, 817, 111
Dutta, et al. 2024b, arXiv:2409.15423
Dutta, S., Muzahid, S., Schaye, J., et al. 2024a, MNRAS, 528, 3745
Evoli, C., & Ferrara, A. 2011, MNRAS, 413, 2721
Hinton, S., Davis, T. M., Lidman, C., Glazebrook, K., & Lewis, G. 2016, A&C, 15, 61
Ho, S. H., Martin, C. L., Kacprzak, G. G., & Churchill, C. W. 2017, ApJ, 835, 267
Ho, S. H., Martin, C. L., & Schaye, J. 2021, ApJ, 923, 137
Huang, Y.-H., Chen, H.-W., Shectman, S. A., et al. 2021, MNRAS, 502, 4743
Inami, H., Bacon, R., Brinchmann, J., et al. 2017, A&A, 608, A2
Johnson, S. D., Chen, H.-W., & Mulchaey, J. S. 2015, MNRAS, 449, 3263
Kacprzak, G. G., Churchill, C. W., Ceverino, D., et al. 2010, ApJ, 711, 533
Kacprzak, G. G., Muzahid, S., Churchill, C. W., Nielsen, N. M., & Charlton, J. C. 2015, ApJ, 815, 22
Kacprzak, G. G., Vander Vliet, J. R., Nielsen, N. M., et al. 2019, ApJ, 870, 137
Keeney, B. A., Stocke, J. T., Danforth, C. W., et al. 2017, ApJS, 230, 6
Kennicutt, R. C. J. 1998, ApJ, 498, 541
Kewley, L. J., Geller, M. J., & Jansen, R. A. 2004, AJ, 127, 2002
Koplitz, B., Edward Buie, I., & Scannapieco, E. 2023, ApJ, 956, 54
Kriek, M., van Dokkum, P. G., Labbé, I., et al. 2009, ApJ, 700, 221
Liang, C. J., Kravtsov, A. V., & Agertz, O. 2016, MNRAS, 458, 1164
Mathes, N. L., Churchill, C. W., Kacprzak, G. G., et al. 2014, ApJ, 792, 128
Mishra, N., Johnson, S. D., Rudie, G. C., et al. 2024, ApJ, 976, 149
Morrissey, P., Matuszewski, M., Martin, D. C., et al. 2018, ApJ, 864, 93
Moster, B. P., Naab, T., & White, S. D. M. 2013, MNRAS, 428, 3121
Muzahid, S., Kacprzak, G. G., Churchill, C. W., et al. 2015, ApJ, 811, 132
Muzahid, S., Schaye, J., Cantalupo, S., et al. 2021, MNRAS, 508, 5612
Muzahid, S., Srianand, R., Bergeron, J., & Petitjean, P. 2012, MNRAS, 421, 446
Ng, M., Nielsen, N. M., Kacprzak, G. G., et al. 2019, ApJ, 886, 66
Nielsen, N. M., Churchill, C. W., Kacprzak, G. G., Murphy, M. T., & Evans, J. L. 2015, ApJ, 812, 83
Oppenheimer, B. D., Crain, R. A., Schaye, J., et al. 2016, MNRAS, 460, 2157
Oppenheimer, B. D., & Schaye, J. 2013, MNRAS, 434, 1043
Petitjean, P., & Bergeron, J. 1990, A&A, 231, 309
Pointon, S. K., Nielsen, N. M., Kacprzak, G. G., et al. 2017, ApJ, 844, 23
Prochaska, J. X., Weiner, B., Chen, H.-W., Mulchaey, J., & Cooksey, K. 2011, ApJ, 740, 91
Qu, Z., Chen, H.-W., Johnson, S. D., et al. 2024, arXiv:2402.08016
Romano, M., Nanni, A., Donevski, D., et al. 2023, A&A, 677, A44
Rosenwasser, B., Muzahid, S., Charlton, J. C., et al. 2018, MNRAS, 476, 2258
Savage, B. D., Kim, T. S., Wakker, B. P., et al. 2014, ApJS, 212, 8
Stocke, J. T., Keeney, B. A., Danforth, C. W., et al. 2014, ApJ, 791, 128
Stocke, J. T., Keeney, B. A., Danforth, C. W., et al. 2017, ApJ, 838, 37
Tchernyshyov, K., Werk, J. K., Wilde, M. C., et al. 2022, ApJ, 927, 147
Tchernyshyov, K., Werk, J. K., Wilde, M. C., et al. 2023, ApJ, 949, 41
Tremonti, C. A., Heckman, T. M., Kauffmann, G., et al. 2004, ApJ, 613, 898
Tripp, T. M., Meiring, J. D., Prochaska, J. X., et al. 2011, Sci, 334, 952
Tripp, T. M., Sembach, K. R., Bowen, D. V., et al. 2008, ApJS, 177, 39
Tumlinson, J., Peeples, M. S., & Werk, J. K. 2017, ARA&A, 55, 389
Tumlinson, J., Thom, C., Werk, J. K., et al. 2011, Sci, 334, 948
Turner, M. L., Schaye, J., Steidel, C. C., Rudie, G. C., & Strom, A. L. 2014, MNRAS, 445, 794
Werk, J. K., Prochaska, J. X., Cantalupo, S., et al. 2016, ApJ, 833, 54
Zabl, J., Bouché, N. F., Schroetter, I., et al. 2019, MNRAS, 485, 1961